Structured Light Profilometry on m-PTC

Gianluca Marotta [1,*], Paola Sansoni [1], Franco Francini [1], David Jafrancesco [1], Maurizio De Lucia [2] and Daniela Fontani [1]

[1] The National Institute of Optics (CNR-INO), 50125 Florence, Italy; paola.sansoni@ino.cnr.it (P.S.); franco.francini@ino.cnr.it (F.F.); david.jafrancesco@ino.cnr.it (D.J.); daniela.fontani@ino.cnr.it (D.F.)

[2] Department of Industrial Engineering, University of Florence, 50139 Florence, Italy; delucia@unifi.it

* Correspondence: gianluca.marotta@ino.cnr.it

Abstract: In concentrating solar systems, it is essential to study the optical losses of the collectors. A fundamental parameter is the *intercept factor*, namely, the fraction of sunrays reflected by the concentrator that reaches the receiver. Optical profilometry studies the relationship between the collector profile and the *intercept factor*, which influences the collection efficiency. Profilometric analyses were performed on a micro-parabolic trough collector (m-PTC), with reduced sizes and greater mirror curvature than a usual PTC. The proposed technique projects a luminous pattern (structured light) both on the collector with an opaque covering and on a flat reference plane. Measurement set-up and calibration technique were developed for m-PTC. A program coded in Python analyzed the images and reconstructs the mirror profile. The tilted reference plane was reconstructed using an original geometric model and a calibration procedure. The focal length of each parabolic section was calculated, providing information on surface defects in the mirror. An important parameter obtained was the displacement of the focus of the parabola with respect to the ideal position. Using this value, the *intercept factor* was estimated to be 0.89. The proposed technique was validated by comparing the results with an independent profilometric study applied to the same m-PTC.

Keywords: parabolic trough collectors; profilometry; structured light; *intercept factor*; optical measurement; solar energy

1. Introduction

One possibility for the production of renewable energy is represented by the development of systems based on the concentration of sunlight. They are systems in which solar radiation is concentrated by solar mirrors to reach high temperatures in a suitable fluid. The heat produced can be used as thermal energy or can be converted into electricity. The parabolic trough collector (PTC) is one of the most used technologies for concentrating sunlight. Large-scale PTC facilities are used in the current energy market to generate electricity [1]. In these installations, the solar mirrors have large dimensions, with up to a 6 m wide opening (a_w, occupying hundreds of hectares of land). On the other hand, solar collectors for the production of medium-temperature heat (150–250 °C) may have small dimensions, with an opening from about 400 mm up to about 2 m, suitable for installation in smaller areas or even on the roofs of buildings.

Alternative technologies have already been proposed, such as direct steam generation for industrial applications, as well as other PTC solutions operating at medium–low temperatures. These have mostly the same problems as PTCs for concentrating solar power (CSP) applications without the advantages of reducing size [2]. On the other hand, in solar heating and cooling applications, the further lowering of the operating temperature puts the parabolic collectors in competition with stationary collectors [3].

In recent years, several researches were carried out on these systems [3–8], and commercial products were also developed [9–13]. In this context, the University of Florence has developed a new design for a micro-PTC (m-PTC), which is a PTC ten smaller than a common PTC; the m-PTC is schematically illustrated in Figure 1.

The development of the m-PTC aims to demonstrate the dimension scalability of PTC technology. Its purpose is to allow the production of heat and electricity directly at the end-user, for industrial and residential purposes. In particular, the optical design chosen gives the mirror the peculiarity of having a rim-angle (ϕ) larger than 90°; in practice, the profile of the concentrator is a parabola with the focus under the mirror opening. The rim-angle (ϕ), highlighted in red in Figure 1, is the angle delimited by the line connecting the focal position with the vertex of the parabola and the line connecting the focus to the mirror edge. This design permits having a compact object, easy to be installed in areas with limited ground surface. Furthermore, the choice of this angle was made to maximize the optical efficiency of the system, considering the random error that could lower this value. Optical efficiency is more shape-sensitive in a micro-PTC. In fact, considering a defect of the same size on the surface of a micro-PTC collector and on a conventional PTC mirror will result in a greater loss of energy on the smaller concentrator, because it affects a larger fraction of the total area of the receiver.
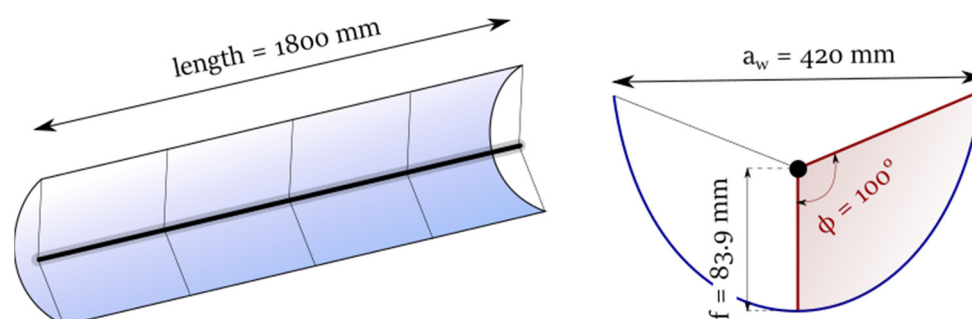
Figure 1. Simplified scheme of the micro-parabolic trough collector (m-PTC) designed by the University of Florence. Length, aperture width (a_w), focal length (f), and rim-angle (ϕ) are reported.

In the current testing phase for this technology [14–17], a fundamental parameter to be experimentally determined and calculated is the optical efficiency of the system. It represents the upper limit that overall efficiency can be reached in the absence of thermal losses. In general, it depends on the angle at which the sun hits the collector. In conditions of a zero angle of incidence, the optical efficiency is defined as

$$\eta^{opt}{}_0 = \rho \cdot \tau \cdot a_r \cdot \gamma, \tag{1}$$

where ρ is the reflectivity of the mirror, a_r is the absorbance of the receiver tube, τ is the transmittance of the glass envelope around the receiver, and γ is a geometric parameter called *intercept factor*.

The *intercept factor* is defined as the fraction of solar rays which, after being reflected by the mirror, can reach the absorber tube placed around the focus of the parabola. The maximum value for this γ ratio is uniquely influenced by the manufacture of the mirror and its correspondence to the design. The presence of defects on the profile of the collector could significantly affect the *intercept factor* and reduce the overall efficiency of the system. For this reason, surface quality control on prototyped collectors is essential for the optimization of these energy systems.

There are several aspects that influence the real value of γ [18]; some of the most important are the physical position of the receiver with respect to the mirror, the actual geometric shape of the concentrator, and alignment of the system with respect to the sun. The last issue is due to the accuracy of the solar tracking system, but the other two are closely related to the mechanical construction of the concentrator. Therefore, it is very important to take them into account to calculate the real optical efficiency of each mirror produced. Furthermore, their consideration could also be useful for solving mechanical problems that can systematically affect the shape of the mirror and, therefore, the

efficiency of the system. For these reasons, an accurate study of the concentrator profile is necessary both in the design phase of new collectors and in their production phase.

Profilometry is the technique used to determine the shape of the mirror surface. In particular, if optical principles and optical instrumentation are applied, it is called optical profilometry. By applying these methods, it is possible to reconstruct the spatial coordinates of the surface and the local slope in order to identify any defects on the profile of the collector. Several techniques are in use for current solar collectors. Optical profilometry can be applied as a technique for the reconstruction of the real shape (profile) of industrial objects without the use of contact measuring devices. In recent years, various optical profilometry techniques were developed on CSP (concentrating solar power) concentrators, in order to obtain a precise calculation of the optical efficiency of CSP systems. There are techniques based on photogrammetry [19,20], on the reflection of a structured pattern [21–23], on laser scanning [24–26], and on the reflection of the image of the receiver tube [27–30].

However, these techniques need to be adapted for each concentrator, which may be of a different shape, have peculiar dimensions, or have special characteristics. They can also fail for specific mirrors, as explained in the sections below.

2. Methodology

2.1. Profile Detection of Micro-PTC

The development of a new PTC prototype required the study and testing of specific profilometry techniques suitable for linear parabolic concentrators and adapted to the small size of the m-PTC examined. Referring to Figure 1, the dimensions of the m-PTC under test were as follows: length, l = 1800 mm; aperture, a_w = 420 mm; focal length, f = 83.9 mm; rim-angle, ϕ = 100°. In the application of profilometry on the m-PTC, several problems arose from its particular geometry, mainly due to the rim-angle being greater than 90°, i.e., with the focus of the parabola within the volume of the reflector. The light hitting the mirror could be reflected twice by the mirror surface, as shown in Figure 2. If this happens, the study of the reflected ray is not related to a single point on the reflector surface. Figure 2 provides an example for hypothetical application of deflectometry on a micro-PTC. The reflected ray represented by the green line reaches the camera after being reflected in two points of the surface and the deformation of the fringe pattern depends on both reflections. An analysis of the fringe pattern cannot, therefore, distinguish defects related to the two points of reflection. Furthermore, the curvature of the mirror varies drastically for the different zones of the mirror, giving considerable variations in the deformations that the surface could cause on reflected objects, raising difficulties in the application of methods using the analysis of the image reflected by the receiver tube.
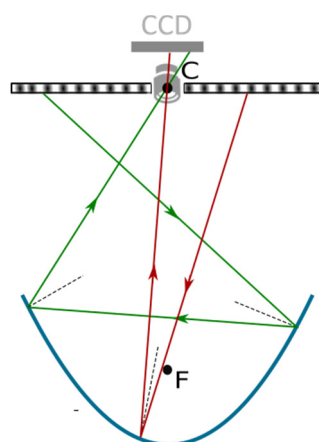

Figure 2. Example of double reflection in an m-PTC for a hypothetical application of deflectometry. F is the focal point of the parabola; C represents the entrance aperture of the camera lens.

Despite these problems, the possibility of measuring the m-PTC shape with imaging techniques need not necessarily be discarded. Considering the various advantages, such as speed of

measurements and ease of set-up, it is worth exploring a different possibility for imaging profilometry. A possible solution to overcome the problem can be to cover the mirror with an opaque, nondestructive material, which avoids reflection. With this configuration, it is possible to project a structured light (i.e., a light with a well-defined pattern) onto the sample. The deformation on this pattern induced by the sample is captured with an acquisition device (a digital single-lens reflex (DSLR) camera). Appropriate geometric calculations could then provide a reconstruction of the shape of the mirror. This technique derives from a well-established method of object profilometry called structured light profilometry (SLP).

2.2. General Principle

In structured light profilometry, a detailed review of which is reported in [31], an important role in the history of optical tests was played by Moiré profilometry [32,33]. In this technique, the structured pattern is formed by alternating black and white straight lines called the Moiré pattern. In classical Moiré profilometry, information is provided starting from the optical interference induced by placing a demodulation grid, identical but slightly misaligned with respect to the original projection grid, between the object and the camera. From the resulting interference pattern, contours of equal height can be extracted. However, the practical aspect of physically putting a demodulation grid can complicate the hardware configuration of the experimental set-up.

Nevertheless, structured light profilometry [31] with a Moiré pattern can also be performed without the presence of the demodulation grid. In this case, the surface height is extracted directly from the analysis of the deformed pattern [26]. With the absence of a demodulating grid, the technique becomes easier to implement, without a lack of accuracy in shape reconstruction.

In the diagram presented in Figure 3b, the unknown data are the height of the object under inspection (Z_H). P and F represent the exit aperture of the projector lens and the entrance aperture of the camera lens, respectively, in a pinhole camera representation. In this case, the optical elements have to be located properly, and, to simplify the calculation, some peculiar alignments are required. The case of literature shown in Figure 3 is interesting to discuss. First of all, P and F have to be at the same distance (L) with respect to the reference plane. Secondly, the optical axis of both camera and projector intersect the plane R at the same point (O). The information about the height of the object Z_H is then evaluated by triangulation. The image of the pattern is recorded on a reference plane (plane R, at z = 0) in the absence of the object under discussion. B is the point that the camera records in presence of that object, while A is the point recorded with its absence. From the similitude between triangles PHC and BHA, it is possible to obtain the desired information about the shape of the object. However, P and F are virtual points that come from approximating the lens as pinholes; thus, they could be difficult to locate and align in real space. This could raise large errors in the object reconstruction. The proposed technique is able to overcome these difficulties, with a different geometric approach and a suitable calibration procedure.
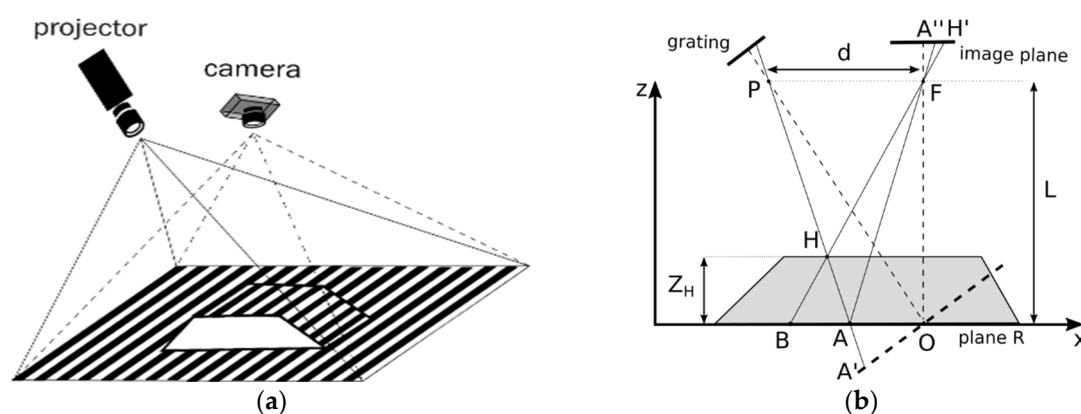

Figure 3. Example of structured light profilometry: (**a**) schemes of the approach and (**b**) geometry of projection and vision systems. Adaptation from [33].

2.3. Experimental Set-Up

To perform SLP on the sample of m-PTC under investigation, the first step was to cover the mirror with a white, diffusive, opaque covering. For this reason, since there was a covering layer deposited by the manufacturer on the mirror surface, white sheets of tissue paper were adhered to the layer that covers the mirror. No damage was reported on the mirror surface and the opaque layer could be removed very easily after performing the experiment. Figure 4 reports a scheme of the experimental set-up. The Moiré pattern was projected both on the "mirror sample" (SA) and on a flat reference plane (RP) placed in front of it. Figure 4a also shows the coordinates of the reference system used in the following calculation. The mirror sample was placed in a vertical position, fixed to a rack, as visible in the photo of the laboratory set-up in Figure 4b. The longitudinal direction was aligned using the gravity with the help of a digital inclinometer. The accuracy of this alignment was coincident with the sensitivity of the device, which was 0.1°. The utilized projector was Newport MP-1000 A, which was placed on a photographic tripod, permitting its alignment. The mounted objective was a Nikkor lens with a focal length of 60 mm. The distance of two consecutive lines of the Moiré pattern, i.e., the period of the grating, was about 9 mm on RP and SA.
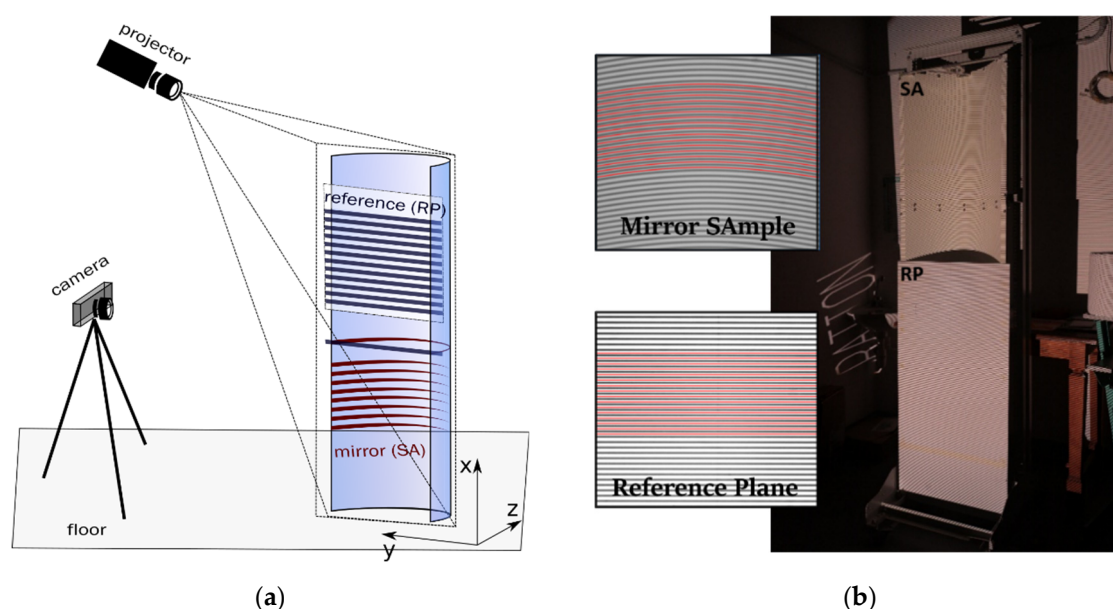

| (**a**) | (**b**) |

Figure 4. Example of structured light profilometry: (**a**) schemes of the approach and (**b**) geometry of projection and vision systems.

The images were taken with a DSLR camera Nikon D7000 using a Nikkor objective with a focal length of 55 mm. The camera had a CCD (charge-coupled device) sensor of 16.9 MP. It was placed at a distance of about 4.25 m, mounted on a tripod that allowed orienting the plane of the CCD parallel to the vertical axis obtained using gravity. The distance was chosen in order to have a complete image of the sample. The orientation was realized using the bubble levels integrated on the tripod. Further alignment was performed by placing the optical axis of the camera perpendicular to the opening of the parabola. Thanks to the symmetry of the object, the camera was considered aligned when the distance between the mirror edge and the camera edge was the same for both the left and the right sides. Concerning the alignment of the projector, the only requirement was that, on the RP plane, the lines of the pattern had to be parallel to the horizontal section of the mirror, i.e., the *y*-axis. For this purpose, a horizontal line was drawn on RP and the projector was displaced until the lines of the Moiré pattern were parallel to the traced line. As Figure 4b shows, the dimensions of RP did not permit covering the entire surface of the sample. To bypass this inconvenience, two photos were taken, with the RP placed on the "top" and "bottom" of the SA.

All numerical calculations and image analyses were performed with suitable Python software developed by one of the authors.

2.4. Geometry of the Reconstruction

A geometric scheme of the set-up is shown in Figure 5, in which a *xz*-section is represented. The projector can be identified with the point P, which corresponds to its exit aperture. This simple scheme considers that each ray exiting from this device passes through this point. Each ray coming from the projector hits the RP plane at a precise point (A) and then the SA plane at the point A'. From the similarity between the triangles PKA and AHA', it is possible to write

$$A'H = PK \cdot \frac{AH}{AK}. \tag{2}$$

The key variable in this equation is the distance AH, here called deformation, δ. It represents the *x*-variation between the points of the line projected on RP and the same points of the same line on SA, as illustrated in Figure 5. Considering that $A'H$ represents the *z*-coordinate of each point on SA (with $z = 0$ on RP), PK is the distance between projector and RP (d_P), and AK is the coordinate of A on the RP plane, if the zero is placed in correspondence with the P-position (x_{RP}), Equation (2) becomes

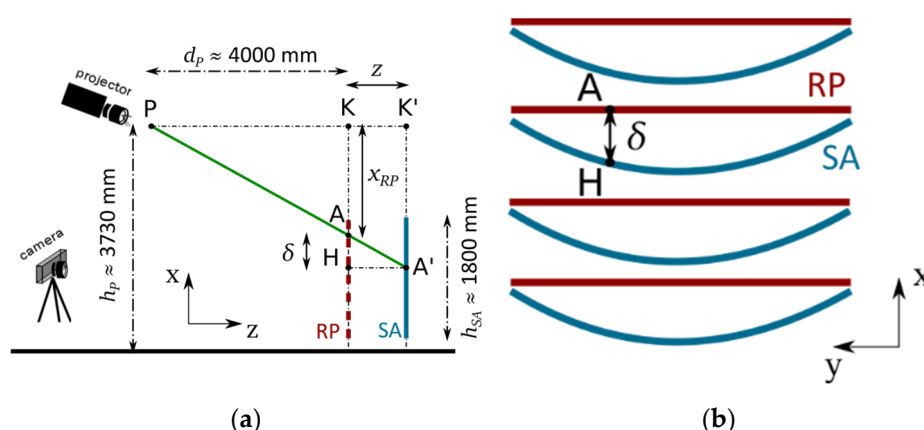$$z(x,y) = d_P \cdot \frac{\delta(x,y)}{x_{RP}(x,y)}. \tag{3}$$

Figure 5. (**a**) Scheme of the geometry behind the reconstruction formula. (**b**) Definition of the deformation, as the distance (along the *x*-axis) between the line projected on reference plane (RP) (red line) and the line on mirror sample (SA) (blue line).

- Unfortunately, Equation (3) is useless for the profile reconstruction. In fact, it considers distances in the real space of the laboratory (*xyz* coordinate system) and it does not take into account the acquisition device (the camera). In fact, the technique is based on the measurement of quantities obtained via photo-acquisition, namely, in the flat reference system of the CCD sensor (*x*y**—reference system). From now on, we refer to quantities in the CCD system with the star-superscript (*). In particular, δ^* and $x_{RP}{}^*$ are the quantities measured with the image analysis. A suitable Python software was developed to individuate and enumerate the lines on SA and RP and to calculate the required quantities.

As for the projector of Figure 5, the camera lens could be schematized as a geometric point (F) corresponding to the system entrance opening (pinhole approximation). In this simple scheme, the image of each point in the space was derived from the intersection between the straight line that connects it to point F and the plane of the CCD sensor. The projection of the significant points on the CCD sensor surface is represented in Figure 6.

For distances measured on a plane parallel to the CCD sensor, their correspondent projections on the CCD sensor were related to them using a simple proportionality. With reference to Figure 6, the segment A^*C^* on the sensor is the projection of the segment AC on RP. By similitude of triangles ACF and A^*C^*F, it is possible to write

$$A^*C^* = c \cdot AC, \tag{4}$$

where $c = \frac{FC^*}{FC}$. Extending this concept, it is possible to write

$$\delta^*(x, y) = c \cdot \delta(x, y), \tag{5}$$

and

$$x_{RP}^*(x, y) = c \cdot x_{RP}(x, y). \tag{6}$$

However, the picture of SA shows the Moiré pattern on the SA plane and not its projection on RP. In other words, the camera captures the point A' and not the point H, which is of interest. Practically, the deformation that can be measured is the segment A'^*A^* (Figure 6), also identified as δ'^*. It can be written as

$$\delta'^*(x, y) = \delta^*(x, y) + \Delta(x, y), \tag{7}$$

where $\Delta(x, y)$ is the segment A'^*H^* in Figure 6. Considering Equations (3) and (5)–(7), the reconstruction formula becomes

$$z(x, y) = d_P \cdot \left[\frac{\delta'^*(x, y) - \Delta(x, y)}{x_{RP}^*(x, y)} \right] = d_P \cdot \left[\frac{\delta'^*(x, y)}{x_{RP}^*(x, y)} + v_z(x, y) \right]. \tag{8}$$

In this formula, z refers to measurable quantities except for $v_z(x, y)$, whose assessment needed to be the object of a study. This correction is named the *vertical-parallax correction*. Furthermore, the distance d_P needed to be calculated, since it was impossible to accurately measure it in laboratory. The calibration procedure, explained below, allowed its estimate.
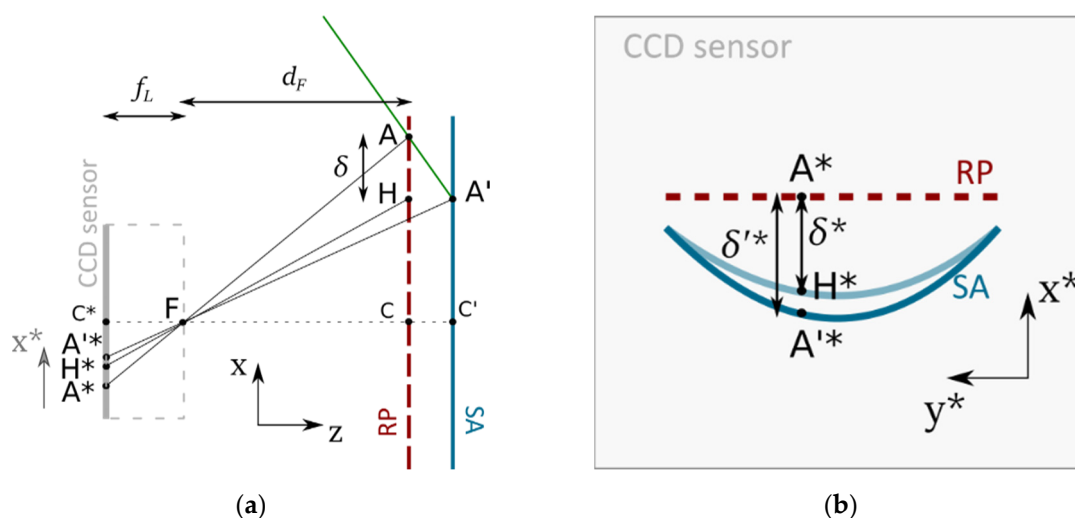

(a)　　　　　　　　　　　　　　　　　　(b)

Figure 6. (**a**) Scheme of the geometry behind the reconstruction formula. (**b**) Definition of the deformation, as the distance between the line projected on RP (red line) with respect to that projected on SA (blue line).

There are other difficulties that can occur while performing spatial measurements by image acquisition; an interesting aspect arises considering the xy-section of the reconstruction scheme. An error could arise in the y-coordinate and, as with the vertical-parallax correction, it is due to the displacement of the apparent position of plane SA with respect to that of plane RP. In particular, for the same x^*y^*-position on the CCD sensor, points of RP and SA will have a different y-coordinate in the xyz reference system. This is due to the fact that rays converge into the lens system of the camera (nonparallel rays). Figure 7 shows a scheme of this effect. It can be easily seen that, for a generic reconstructed point (as A in Figure 7),

$$y = y_{RP} + \delta y. \tag{9}$$

In the reconstruction procedure, the measure concerns the deformation δ'^* for points that have the same y^*-coordinate in RP and SA images. Its value is

$$y^* = c \cdot y_{RP}. \tag{10}$$

From Equations (9) and (10), the y-coordinate of reconstructed points becomes

$$y = \frac{y^*}{c} + \delta y = \frac{y^*}{c} + \frac{z \cdot y_{RP}}{d_F}, \tag{11}$$

where the value of δy is obtained using a simple calculation of trigonometry with the lengths indicated in Figure 7. The last term of Equation (10) is named *non-parallel ray correction*. As the formula shows, it strictly depends on the measure of the camera position d_F and varies for different values of z and y.
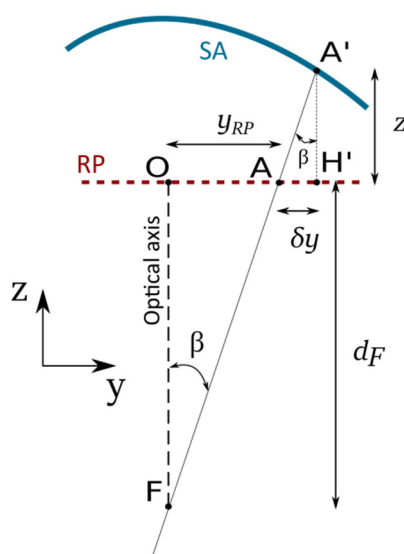

Figure 7. Geometric scheme to estimate the nonparallel ray correction.

To measure the quantity d_F the principle used is that distances on planes are proportional to the distances on the projected image on the CCD sensor. Considering the height of the mirror $h_{SA} = 1800$ mm, and the value of its projection on the CCD, $h^*_{SA} = 20.5$ mm, then

$$d_F = \frac{f_L \cdot h_{SA}}{h^*_{SA}} - w_{RP}, \tag{12}$$

where f_L is the focal length of the camera lens, and $w_{RP} = 6$ mm is the effective width of the reference plane. Unlike the vertical parallax, this correction is completely defined with the calculation of d_F.

2.5. Vertical-Parallax Correction

In order to perform the reconstruction of the shape of the mirror, the term of the vertical–parallax correction ($v_z(x, y)$ in Equation (8)) had to be estimated. To understand its behavior, it was useful to perform the reconstruction with $v_z = 0$. As Figure 8 shows, the shape of the collector seemed to be affected by a systematic error. The z-coordinate seemed to be greater for smaller values of the x-coordinate, giving the parabola a deformed shape that was clearly different from the real one. To perform the reconstruction shown in Figure 8, the correct value of the projector–RP distance (d_P) was considered. The procedure to measure d_P is explained in the next section.
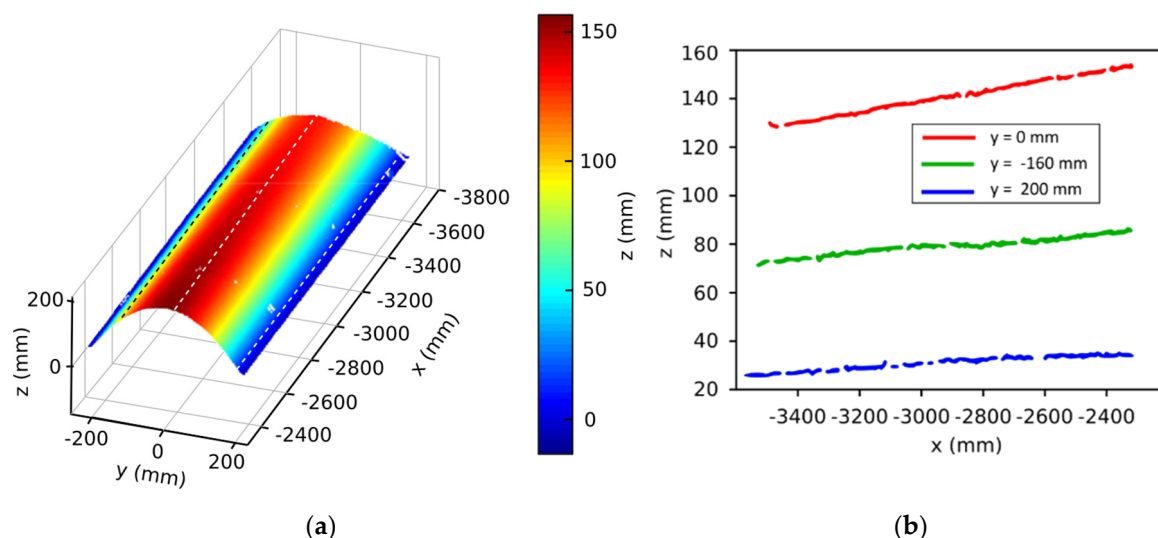
(**a**)　　　　　　　　　　　　　　　　　(**b**)

Figure 8. (**a**) Reconstruction of m-PTC without performing the vertical-parallax correction. (**b**) Section of the reconstructed profile for three different values of *y*, indicated by dashed lines in (**a**).

If longitudinal sections (parallel to the *x*-axis) were plotted, as in Figure 8b, it was easy to note that the behavior of the *z*-coordinate was not constant, as expected, but it could be approximated, empirically, with a linear function. Furthermore, sections corresponding to greater values of *z* were more deformed than those with lower *z* value. In general, it is possible to write

$$v_z(x, y) = m_z(y) \cdot x + q_z(y), \tag{13}$$

where the parameters $m_z(y)$ and $q_z(y)$ are different for each *y*-section. The subscript *z* underlines that their value is strictly dependent from the *z*-value.

As can be inferred from Figure 8, the value of m_z increased for greater values of z, corresponding to the inclination of the fitting line with respect to the *x*-axis. It appeared as a property of the parallax error; in fact, if the error was always zero in correspondence with the camera position, it grew for increasing values of z. On the other hand, for the same reason, the value of q_z was the *z*-coordinate of the point positioned at the same height of the camera, where the parallax had zero value. This happened for $x = x_F = 952$ mm, corresponding to the *x*-coordinate of the point F. This value was calculated with the same procedure for the measure of d_F, i.e., the distance of RP from F. With a linear fitting of the *x*-sections, it was possible to evaluate the quantities m_z, q_z for each section and, thus, v_z. The correction found was not valid for any shape to be reconstructed, because of its dependence on z; however, this calculation showed its functional form. For objects with a well-known longitudinal section (e.g., SA), it is always possible to infer its entity.

2.6. Calibration Procedure

The difficulty in measuring the position of P was already mentioned, since it is a virtual point located almost at the exit aperture of the projector lens. It is impossible to locate it, and a direct measurement would cause a very large uncertainty on the profile reconstruction, as can be inferred from Equation (8). For this reason, a calibration procedure was developed.

The principle was to match the orientation angle of a reconstructed plane to the known tilt angle of the reference plane in space. For this aim, the same RP plane was tilted of an angle α around the *x*-axis, as presented in Figure 9. A variation in the α-value corresponds to a variation in the overall *z*-values of the reconstructed surface. In the case of a tilted RP, this means that, upon varying the projector–RP distance (d_p), the angle of tilt (α) would be different.

To calculate the value of α in the reconstructed surface, linear fits were made for the fixed *y*-sections and the angle was evaluated as the average value of these angular coefficients. Therefore, the surface was reconstructed for different values of d_P, and the corresponding values of the tilt angle

α were calculated, as illustrated in Figure 10a. The value that gave the correct reconstruction, i.e., its real measure, was taken as corrected. Since, in the laboratory, a value of α = (20.298 $\pm$ 0.005)° was measured, the distance of the projector was inferred to be d_p = (3974.5 $\pm$ 0.5) mm, as reported in Figure 10.
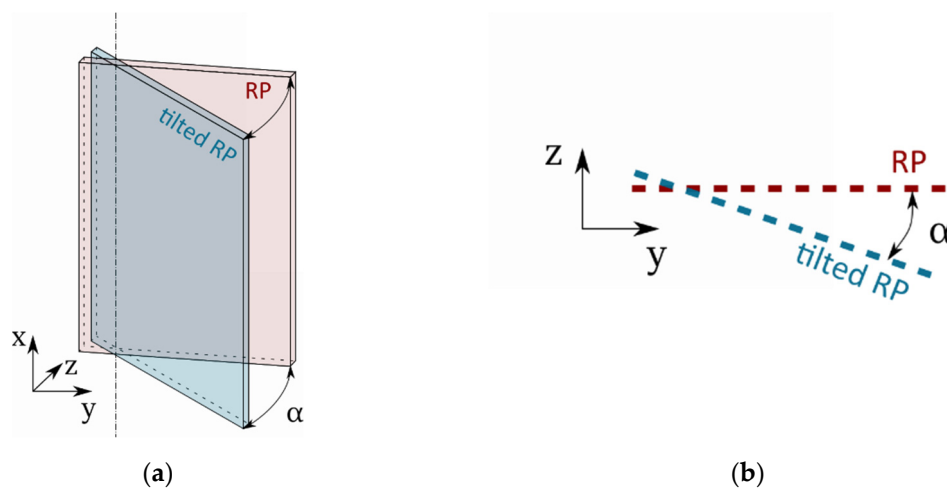

(a)   (b)

Figure 9. Scheme of the tilted RP: (**a**) three-dimensional (3D) view and (**b**) top view.
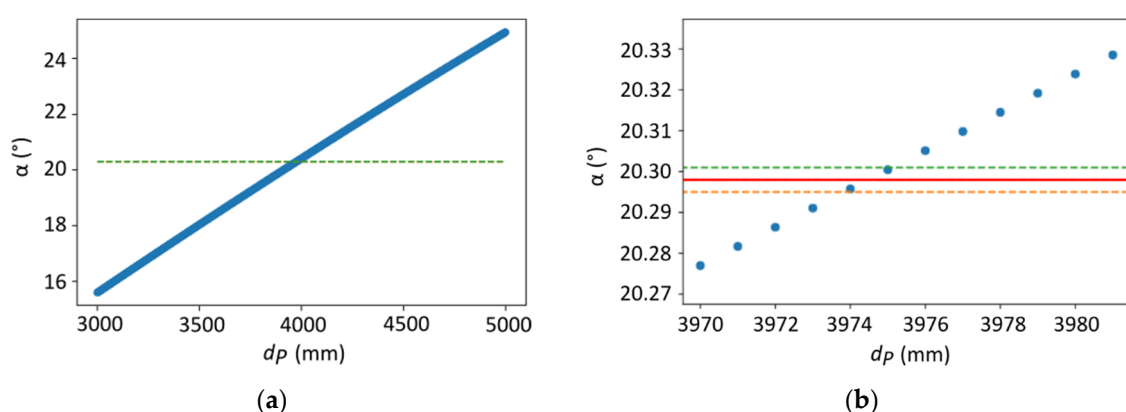

(a)   (b)

Figure 10. (**a**) Variation of the tilt angle in the reconstructed tilted RP for different virtual positions of the projector. The dashed line indicates the real value of the tilted angle. (**b**) Detail of the graph shown in (**a**) in proximity of the real value of d_P. The straight line indicates the expected value of tilt angle, while the dashed lines indicate its uncertainty interval.

3. Results

3.1. Reconstruction of the Mirror and Focus Estimate

Once all parameters in Equation (8) were determined, it was finally possible to reconstruct the surface of the m-PTC. Figure 11 presents the reconstruction of the surface of the micro-PTC and the tilted RP used for calibration.

After that, the reconstruction of the mirror was provided; it was important to extract information about the quality of the manufacture of its surface. Unfortunately, the "noise" data due to the uncertainty of the method did not allow a direct estimation of the slope error on the surface. A parameter that could explain the global deformation of the mirror is the displacement of the focus of each parabolic section.
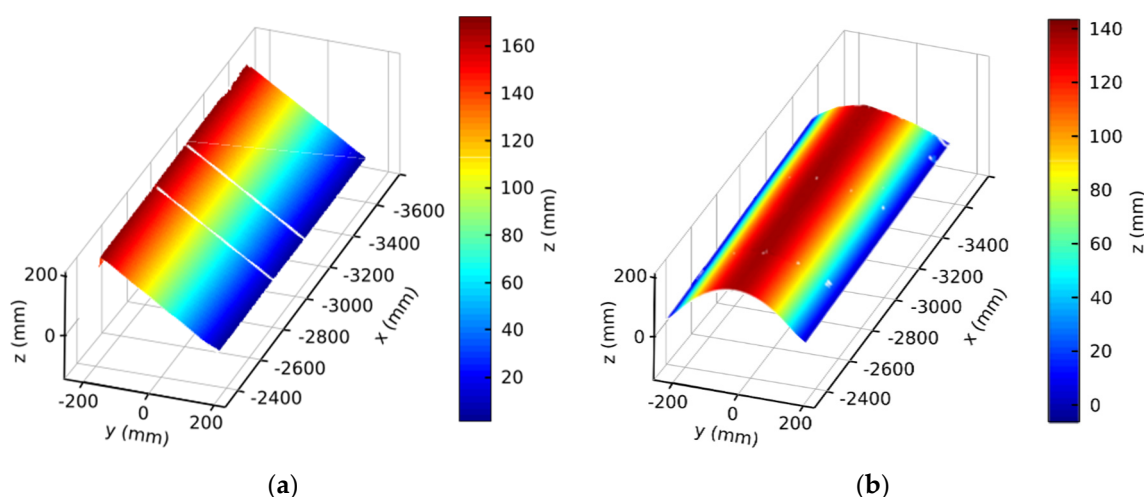
(**a**)   (**b**)

Figure 11. Reconstruction of the reference plane (**a**) and of the m-PTC (**b**).

To achieve the measurement of the focal length for each parabolic section, the data from the reconstruction were fitted with the following parabolic function:

$$z = a \cdot y^2 + b \cdot y + c. \tag{14}$$

Knowing the parameters of the fit (a, b and c), the coordinates of the focus (y_F, z_F) were calculated as follows:

$$y_F = \frac{-b}{2a} \; ; \; z_F = \frac{1 - b^2 + 4ac}{4a}, \tag{15}$$

while the coordinates of the vertex (y_V, z_V) could be obtained as follows:

$$y_V = \frac{-b}{2a} \; ; \; z_V = \frac{-b^2 + 4ac}{4a}. \tag{16}$$

Therefore, the focal length was

$$f = |z_F - z_V| = \left| \frac{1}{4a} \right|. \tag{17}$$

Figure 12 shows the results of the calculations of vertex, focus, and focal length for the whole collector. It is worth noting the presence of a little "step" around $x = -2600$ mm. In fact, this step was in correspondence with the junction between the mirror and its supporting structure, where two different parts of the reflector were jointed (the actual junction is visible in the photo of Figure 4b, in correspondence with the screws). In correspondence with this "step", the vertex position fluctuated by about 0.5 mm. This number was consistent with a direct measure made with a caliber. The presence of this irregularity on the mirror surface due to a junction structure and its correct detection by the SLP technique confirmed the reliability of the technique. At the same time, it gave an estimate of the accuracy in the measurement of focus position and focal length, which needed to be at least of the order of this defect, i.e., 0.5 mm. Considering the 95% bound confidence for the parameters of the fit, it was possible to estimate the uncertainty of the three examined quantities. The mean uncertainty was 0.12 mm with a standard deviation of 0.06 mm. Table 1 reports the mean value of the measured quantities with their standard deviation.

Table 1. Result of SLP (structured light profilometry) on m-PTC (micro-parabolic trough collector).

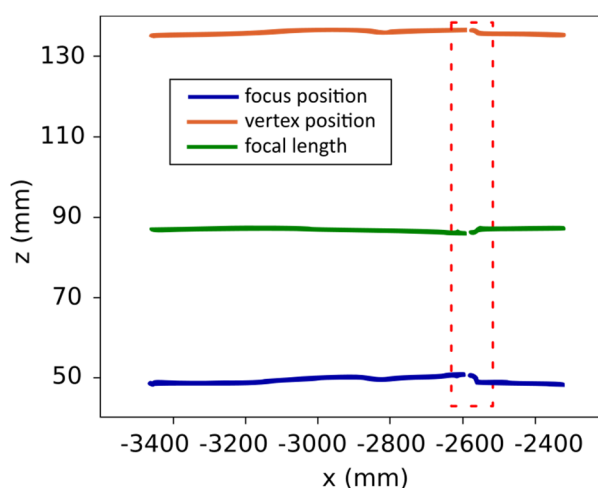| Vertex Position (mm)	Focus Position (mm)	Focal Length (mm)
136.2 ± 0.5	49.3 ± 0.8	86.9 ± 0.3

Figure 12. Focal length, focus, and vertex positions calculated for each parabolic section of the reconstructed profile. The dotted square indicates the presence of a "step" in the longitudinal section.

3.2. Estimation of the Intercept Factor

The *intercept factor* (γ) is defined as the fraction of sunrays which, after being reflected by the mirror, can reach the absorber tube in the parabola focus). The maximum value of γ essentially depends on the manufacture of the solar mirror and its correspondence to the design. As discussed in the introduction, γ is the parameter that includes all geometric errors and that contributes to the calculation of the optical efficiency. In practice, the collector features that mostly influence the γ value are the receiver position referring to the mirror, the real m-PTC profile, and the solar alignment of the system.

Güven and Bannerot gave a theoretical model for the γ estimation in 1986 [18]. In this model, the *intercept factor* is calculated as a function of various parameters.

$$\gamma = f\left(\phi, C_R, D, \sigma_{tot,r}, \beta, d_z\right), \tag{18}$$

where ϕ is the rim-angle, C_R is the concentration ratio, D is the diameter of the absorber tube, $\sigma_{tot,r}$ the value of the random error, treated as the variance of Gaussian distributions, β is the reflector misalignment with respect to the solar radiation, and d_z the receiver displacement along the optical axis. Using this last variable, they demonstrated that the receiver displacement along the optical axis (z in Figure 3) degrades the optical performance more than the displacement along the y-axis. Furthermore, they demonstrated that a single parameter, d_z, can account for both receiver location and reflector profile errors. In the examined case of the m-PTC, receiver location errors were not taken into account; on the other hand, the focus displacement was retrieved as the global parameter for the deformation of the mirror and, thus, the quality of the manufacture.

Confronting the results presented in Table 1 with the designed ones, it can be seen that the measured focal length differed by about 3 mm from the designed collector. An estimate of the *intercept factor* was then possible, by putting this value as focus displacement (d_z) in the theoretical model. To perform the calculation, designed values for C_R and D were provided, while, to evaluate the random errors, we imposed $\sigma_{tot,r}$ = 15 mrad. This last value was the estimation of such errors used in the optical design of the system. For d_z = 3 mm, the calculation gave the value of γ = 0.89. In this calculation, misalignment errors were not considered (β = 0), since the purpose of the method was to evaluate errors derived only from the shape of the mirror.

It is worth noting that these values came from a technique where the profile of the mirror was approximated with a quadratic function. It was not able to estimate the local contribution to the *intercept factor*, and all the errors were summarized in the focal length calculation. However, the estimation of the *intercept factor* without considering the local slope error is a good parameter to evaluate the quality of the manufacture. The present technique can be useful used to compare different prototypes of m-PTCs. Furthermore, with respect to laser profilometry, it represents a faster surface control under reproducible conditions and in an easily assessable environment.

Referring to the design values, the maximum *intercept factor* for the prototype should be 0.91. In that calculation, the same random errors $\sigma_{tot,r}$ were considered. By comparing this result, the SLP profilometry was able to provide an estimate of optical losses due only to the manufacture of the mirror profile.

3.3. Validation

The proposed method, based on structured light profilometry, was validated by measuring the same parameters with a different technique in a completely independent measurement on the same sample. The validation technique was based on laser scanning and it was applied on the same micro-parabolic trough collector to assess the *intercept factor*. In the latter technique, a laser beam hit the mirror perpendicular to its aperture plane and then it was reflected on a target placed on the focal point of the mirror. A camera took pictures of the target, allowing measurement of the position of the reflected spot with respect to the focal line. The laser scanning technique referred to the same *xyz* system shown in Figure 4a. For each *x*-position, a scan along the *y*-position was performed, and the *z* position and the slope were iteratively calculated. This laser scanning technique was discussed with additional detail in [17].

After having calculated the *z*-position and the slope, it was possible to estimate the *intercept factor* of the surface under examination. Geometric calculations determined if a ray, after entering the parabola opening, being reflected by the surface element under estimation, could reach the absorber tube placed in its ideal position. The sum of all surface elements that satisfied this condition, divided by the entire surface, defined the *intercept factor*. To obtain a more adequate value, random errors ($\sigma_{tot,r}$) were also considered in the calculation.

In conclusion, the validation technique assessed the *intercept factor*, with a measurement procedure completely independent from the structured light profilometry method. The value obtained was 0.89, in perfect agreement with that presented in Section 3.1, confirming the validity of the SLP method presented in this paper.

4. Conclusions

Profilometry measurements are useful to detect surface faults on solar concentrators, especially for linear parabolic mirrors, which can be imperfectly manufactured. A new prototype of a micro-PTC was optically designed and realized at the University of Florence. The m-PTC has a length of 1800 mm, a collector aperture of 420 mm, a focal length of 83.9 mm, and a rim angle of 100° (focus under the mirror aperture). The surface manufacturing was identified as crucial to system performance. The peculiar dimensions and shape of this micro-PTC made it necessary to re-adjust the structured light profilometry (SLP) detection on an opaque mirror covering.

The main steps of the described work were as follows:

- Design of a suitable set-up able to perform measurements of the whole surface, avoiding the acquisition of multiple images.
- Development of a calibration technique in order to take into account the position of the optical elements and all the optical corrections needed. Once the calibration was performed, the system was ready for the measurement.
- Reconstruction of the profile analyzing the shape of the Moiré pattern projected on the mirror surface in comparison with the reference one.
- Calculation of the focal length of each parabolic section. The analysis of these values could be used to find macroscopic surface errors.
- Computation of the *intercept factor* using a well-known theoretical model. The result of this calculation was 0.89. Unfortunately, this technique was not able to calculate the local contribution to the *intercept factor* or the origin of the optical losses. The *intercept factor* was then estimated as a result of the average surface quality of the collector. However, this value could be compared with maximum *intercept factor* expected in the design, i.e., 0.91, giving the amount of optical loss due only to the manufacture of the mirror profile.

- Validation, considering a profilometric study carried out on the same m-PTC sample with a laser scanning technique. The *intercept factor* measured with this validation technique was 0.89. The good agreement between the two results, obtained with two different methodologies in two completely independent measurements, confirmed the reliability of this SLP method.

Compared with laser profilometry, the SLP technique provides very fast analysis. Once the system is correctly calibrated, it is not necessary to acquire new reference images, and several samples can be measured in series. The major drawback is the preparation of the mirror surface.

Furthermore, in an industrial phase, the surface quality control of the solar mirror could be an important value for the reliability of the system. For these reasons, the optical profilometric study of a micro-PTC is an essential tool for an effective and reliable production of these energetic systems.

The micro-PTC was designed with dimensions of the mirror reduced with respect to the usual ones in an effort to minimize costs with an approach similar to that occurring for photovoltaic systems: size reduction and standardization. Promising applications include installations in small areas, for residential and industrial purposes.

This work could be a suggestion to study and develop novel techniques of profilometric measurements for these cases, where there are problems in applying classical profilometry. This lack of research was confirmed by the fact that this topic has never been considered in the literature.

Conflicts of Interest: The authors declare no conflicts of interest.

Nomenclature

Symbol	Quantity
α_r	absorbance of the receiver tube
a_w	aperture width
CCD	charge-coupled device
C_R	concentration ratio
CSP	concentrating solar power
y_V, z_V	coordinates of the parabola vertex
xyz	coordinate system
δ	deformation
D	diameter of the absorber tube
DSLR-camera	digital single-lens reflex camera
d_F	distance between camera and reference plane
d_P	distance between projector and reference plane
L	distance with respect to the reference plane
f	focal length
f_L	focal length of the camera lens
h_{SA}	height of the mirror
Z_H	height of the object from the ground
γ	intercept factor
m_z and q_z	linear approximation parameters
m-PTC	micro-parabolic trough collector
SA	mirror sample
η^{opt}_0	optical efficiency
PTC	parabolic trough collector
RP	reference plane
$\sigma_{tot,r}$	random errors
d_z	receiver displacement along the optical axis
ρ	reflectivity of the mirror

β	reflector misalignment with respect to the solar rays
ϕ	rim-angle
SLP	structured light profilometry
α	tilt angle around the x-axis
τ	transmittance of the glass envelope
$v_z(x,y)$	vertical-parallax correction
F	virtual point that represents the aperture of the camera lens
P	virtual point that represents the objective of the projector
w_{RP}	width of the reference plane
*	corresponding values measured with the camera

References

1. Fernández-García, A.; Zarza, E.; Valenzuela, L.; Pérez, M. Parabolic-trough solar collectors and their applications. *Renew. Sustain. Energy Rev.* **2010**, *14*, 1695–1721, doi:10.1016/j.rser.2010.03.012.
2. Sansoni, P.; Fontani, F.; Francini, F.; Giannuzzi, A.; Sani, E.; Mercatelli, L.; Jafrancesco, D. Optical collection efficiency and orientation of a solar trough medium-power plant installed in Italy. *Renew. Energy* **2011**, *36*, 2341, doi:10.1016/j.renene.2011.02.004.
3. Balghouthi, M.; Ali, A.B.; Trabelsi, S.E.; Guizani, A. Optical and thermal evaluations of a medium temperature parabolic trough solar collector used in a cooling installation. *Energy Convers. Manag.* **2014**, *86*, 1134–1146, doi:10.1016/j.enconman.2014.06.095.
4. Fernández-García, A.; Rojas, E.; Pérez, M.; Silva, R.; Hernández-Escobedo, Q.; Manzano-Agugliaro, F. A parabolic-trough collector for cleaner industrial process heat. *J. Clean. Prod.* **2015**, *89*, 272–285, doi:10.1016/j.jclepro.2014.11.018.
5. Li, Q.; Zheng, C.; Shirazi, A.; Bany Mousa, O.; Moscia, F.; Scott, J.A.; Taylor, R.A. Design and analysis of a medium-temperature, concentrated solar thermal collector for air-conditioning applications. *Appl. Energy* **2017**, *190*, 1159–1173, doi:10.1016/j.apenergy.2017.01.040.
6. Crema, L.; Alberti, F.; Wackelgard, E.; Rivolta, B.; Hesse, S.; Luminari, L.; Hislop, D.; Restall, B.A. Novel system for distributed energy generation from a small scale concentrated solar power. *Energy Procedia* **2014**, *57*, 447–456, doi:10.1016/j.egypro.2014.10.198.
7. Horta, P. Process Heat Collectors: State of the Art and Available Medium Temperature Collectors. IEA SHC Task49/IV—Deliverable A1.3. 2016. Available online: https://task49.iea-shc.org/publications (accessed on 18 May 2020).
8. Zou, B.; Dong, J.; Yao, Y.; Jiang, Y. An experimental investigation on a small-sized parabolic trough solar collector for water heating in cold areas. *Appl. Energy* **2015**, *163*, 396–407, doi:10.1016/j.apenergy.2015.10.186.
9. IT Collect. Available online: http://www.itcollect.de/index.html (accessed on 3 July 2020).
10. NEP Solar. Available online: http://www.nep-solar.com/wp-content/uploads/2013/11/NEP-Solar-Polytrough1800_Datasheet.pdf (accessed on 3 July 2020).
11. Solitem Group. Available online: http://solitermgroup.com/en/content.php?cat=2&content=2 (accessed on 3 July 2020).
12. Inventive Power. Available online: https://inventivepower.com.mx/pdf/data-sheet-110-ingles.pdf (accessed on 3 July 2020).
13. Trivelli Energia. Available online: http://www.seagroupe.com/page12.html (accessed on 3 July 2020).
14. Pierucci, G.; Hosouli, S.; Messeri, M.; Salvestroni, M.; Fagioli, F.; Taddei, F.; Pourreza, A.; Rashidi, H.; De Lucia, M. Realization of a test rig for small solar collectors and preliminary test. *AIP Conf. Proc.* **2019**, *2126*, 120016, doi:10.1063/1.5117634.
15. Pierucci, G.; Hosouli, S.; Salvestroni, M.; Messeri, M.; Fagioli, F.; Taddei, F.; De Lucia, M. Experimental methodology and thermal loss tests on small size absorber tubes for solar applications. *Energies* **2018**, *11*, 2552, doi:10.3390/en11102552.
16. Salvestroni, M.; Pierucci, G.; Fagioli, F.; Pourreza, A.; Messeri, M.; Taddei, F.; Hosouli, S.; Rashidi, H.; De Lucia, M. Design of a small size PTC: Computational model for the receiver tube and validation with heat loss test. *IOP Conf. Ser. Mater. Sci. Eng.* **2019**, *556*, 012025, doi:10.1088/1757-899X/556/1/012025.
17. Marotta, G.; Fontani, D.; Francini, F.; Jafrancesco, D.; Sansoni, P.; Messeri, M.; Pierucci, G.; De Lucia, M. Comparison between two methods of optical profilometry on micro-PTC. *AIP Conf. Proc.* **2019**, *2126*, 120011, doi:10.1063/1.5117629.

18. Güven, H.M.; Bannerot, R.B. Derivation of Universal Error Parameters for Comprehensive Optical Analysis of Parabolic Troughs. *J. Sol. Energy Eng.* **1986**, *108*, 275–281, doi:10.1115/1.3268106.

19. Pottler, K.; Lüpfert, E.; Johnston, G.H.G.; Shortis, M.R. Photogrammetry: A powerful tool for geometric analysis of solar concentrators and their components. *J. Sol. Energy Eng. Trans. ASME* **2005**, *127*, 94–101, doi:10.1115/1.1824109.

20. Shortis, M.R.; Johnston, G.H.G. Photogrammetry: An available surface characterization tool for solar concentrators, part i: Measurements of surfaces. *J. Sol. Energy Eng. Trans. ASME* **1996**, *118*, 146–150, doi:10.1115/1.2870886.

21. El Ydrissi, M.; Ghennioui, H.; Bennouna, E.G.; Farid, A. A review of optical errors and available applications of deflectometry technique in solar thermal power applications. *Renew. Sustain. Energy Rev.* **2019**, *116*, 109438, doi:10.1016/j.rser.2019.109438.

22. Huang, L.; Idir, M.; Zuo, C.; Asundi, A. Review of phase measuring deflectometry. *Opt. Lasers Eng.* **2018**, *107*, 247–257, doi:10.1016/j.optlaseng.2018.03.026.

23. Sansoni, P.; Fontani, D.; Francini, F.; Mercatelli, L.; Jafrancesco, D. Color-coded methodology for deformable mirrors. *Opt. Eng.* **2006**, *45*, 080508, doi:10.1117/1.2333452.

24. Maccari, A.; Montecchi, M. An optical profilometer for the characterisation of parabolic trough solar concentrators. *Sol. Energy* **2007**, *81*, 185–194, doi:10.1016/j.solener.2006.04.004.

25. Sansoni, P.; Fontani, D.; Francini, F.; Mercatelli, L.; Jafrancesco, D.; Sani, E. Profile control on solar parabolic troughs. In Proceedings of the 2014 Fotonica AEIT Italian Conference on Photonics Technologies, Naples, Italy, 12–14 May 2014; pp 1–4, doi:10.1109/Fotonica.2014.6843911.

26. Wendelin, T.; May, K.; Gee, R. Video Scanning Hartmann Optical Testing of state-of-the-art parabolic trough concentrators. In Proceedings of the ASME 2006 International Solar Energy Conference, Denver, CO, USA, 8–13 July 2006; pp. 699–707, doi:10.1115/ISEC2006-99172.

27. Francini, F.; Fontani, D.; Sansoni, P.; Mercatelli, L.; Jafrancesco, D.; Sani, E. Evaluation of surface slope irregularity in linear parabolic solar collectors. *Int. J. Photoenergy* **2012**, *2012*, 921780, doi:10.1155/2012/921780.

28. Prahl, C.; Stanicki, B.; Hilgert, C.; Ulmer, S.; Röger, M. Airborne shape measurement of parabolic trough collector fields. *Sol. Energy* **2013**, *91*, 68–78, doi:10.1016/j.solener.2013.01.012.

29. Ulmer, S.; Heinz, B.; Pottler, K.; Lüpfert, E. Slope error measurements of parabolic troughs using the reflected image of the absorber tube *J. Sol. Energy Eng. Trans. ASME* **2009**, *131*, 0110141–0110145, doi:10.1115/1.3035811.

30. Stynes, J.K.; Ihas, B. Slope error measurement tool for solar parabolic trough collectors. In Proceedings of the 2012 World Renewable Energy Forum, Denver, CO, USA, 13–17 May 2012. Available online: https://www.nrel.gov/docs/fy12osti/54636.pdf (accessed on 3 May 2020).

31. Van der Jeught, S.; Dirckx, J.J.J. Real-time structured light profilometry: A review. *Opt. Lasers Eng.* **2016**, *87*, 18–31, doi:10.1016/j.optlaseng.2016.01.011.

32. Meadows, D.M.; Johnson, W.O.; Allen, J.B. Generation of Surface Contours by Moiré Patterns *Appl. Opt.* **1970**, *9*, 942, doi:10.1364/ao.9.000942.

33. Sansoni, G.; Biancardi, L.; Minoni, U.; Docchio, F. A Novel, Adaptive System for 3-D Optical Profilometry Using a Liquid Crystal Light Projector. *IEEE Trans. Instrum. Meas.* **1994**, *43*, 558–566, doi:10.1109/19.310169.